Chem Soc Rev

Nanoconfining Solution-Processed Organic Semiconductors for Emerging Optoelectronics

Journal:	*Chemical Society Reviews*
Manuscript ID	CS-TRV-05-2021-000430.R1
Article Type:	Tutorial Review
Date Submitted by the Author:	11-Jun-2021
Complete List of Authors:	Zhang, Yuze; Stevens Institute of Technology, Chemical Engineering and Materials Science Chen, Alina; Stevens Institute of Technology, Chemical Engineering and Materials Science Kim, Min-Woo; New York University, Molecular Design Institute, Department of Chemistry Alaei, Aida; New York University, Molecular Design Institute, Department of Chemistry Lee, Stephanie; Stevens Institute of Technology, Chemical Engineering and Materials Science; New York University, Molecular Design Institute, Department of Chemistry

ARTICLE

Nanoconfining Solution-Processed Organic Semiconductors for Emerging Optoelectronics

Received 00th January 20xx,
Accepted 00th January 20xx

DOI: 10.1039/x0xx00000x

Yuze Zhang,[a] Alina Chen,[a] Min-Woo Kim,[b] Aida Alaei,[b] and Stephanie S. Lee[a,b]*

Solution-processable organic materials for emerging electronics can generally be divided into two classes of semiconductors, organic small molecules and polymers. The theoretical thermodynamic limits of device performance are largely determined by the molecular structure of these compounds, and advances in synthetic routes have led to significant progress in charge mobilities and light conversion and light emission efficiencies over the past several decades. Still, the uncontrolled formation of out-of-equilibrium film microstructures and unfavorable polymorphs during rapid solution processing remains a critical bottleneck facing the commercialization of these materials. This tutorial review provides an overview of the use of nanoconfining scaffolds to impose order onto solution-processed semiconducting films to overcome this limitation. For organic semiconducting small molecules and polymers, which typically exhibit strong crystal growth and charge transport anisotropy along different crystallographic directions, nanoconfining crystallization within nanopores and nanogrooves can preferentially orient the fast charge transport direction of crystals with the direction of current flow in devices. Nanoconfinement can also stabilize high-performance metastable polymorphs by shifting their relative Gibbs free energies via increasing the surface area-to-volume ratio. Promisingly, such nanoconfinement-induced improvements in film and crystal structures have been demonstrated to enhance the performance and stability of emerging optoelectronics that will enable to large-scale manufacturing of flexible, lightweight displays and solar cells.

Key learning points

- The performance of emerging optoelectronics based on semiconducting organic small molecules and polymers is intimately tied to the semiconductor microstructure, including crystal size, orientation, and polymorphism.
- Confining semiconductor crystallization on the tens to hundreds of nanometers length scale within nanostructured scaffolds is a promising strategy to optimize their microstructures for different device architectures while retaining compatibility with rapid processing from solution.
- Nanoconfining small-molecule and polymer crystals can preferentially orient their fast charge transport direction parallel to the unconfined dimension of the nanoconfining space and select for high-performance polymorphs.

Introduction

Emerging optoelectronics replace silicon with materials that can be deposited from solution at low temperatures and atmospheric pressure via high-throughput, rapid deposition methods, such as roll-to-roll coating and inkjet printing. Such ease of processing promises to drive down manufacturing costs while increasing the production capacity of flexible, rollable and light-weight devices, including active matrix displays, sensors and photovoltaics. The field of organic electronics began with the discovery and synthesis of conducting polymers, for which Drs. Alan Heeger, Alan MacDiarmid and Hideki Shirakawa were awarded the 2000 Nobel Prize in Chemistry. Over the past several decades, breakthroughs in synthetic routes to design increasingly narrow bandgap polymers and small-molecule organic semiconductors with high solubility in organic solvents, as well as the design of film morphologies, such as the bulk-heterojunction solar cell, have propelled progress in this field.

Despite tremendous progress in the development of devices comprising organic and hybrid semiconductors, organic light-emitting diodes are the only devices in this class of materials currently being manufactured commercially. Issues with stability and morphology control have limited the performance and lifetimes of emerging optoelectronics well below their theoretical capacity. The rapid nature of solution processing in particular, while advantageous from a manufacturing perspective, introduces defects and heterogeneities across multiple length scales that negatively impact optoelectronic processes, including charge transport and exciton dissociation/recombination. During solution-based deposition of optoelectronic active layers, molecular assembly via solution-phase crystallization is limited to the tens to hundreds of seconds time scale needed for solvent evaporation during active layer deposition.

[a] Department of Chemical Engineering and Materials Science, Stevens Institute of Technology, Hoboken, NJ 07030 USA
[b] Molecular Design Institute, Department of Chemistry, New York University, New York, NY 10003, USA. Email: stephlee@nyu.edu

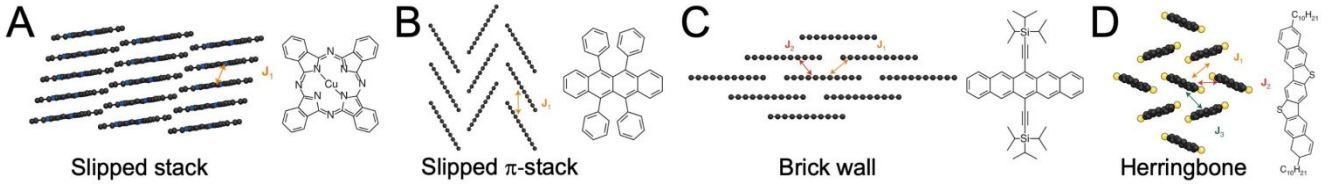

Figure 1. Molecular structures and packing arrangements of four prototypical small-molecule organic semiconductors, including A) copper phthalocyanine, B) rubrene, C) TIPS-PEN and D) C_{10}-DNBT-NW. The dominant transfer integrals, *J*, are displayed for each packing arrangement. Adapted with permission from Ref. 1. Copyright 2020, Nature Publishing Group.

To this end, the use of nanoconfining scaffolds is being actively explored as a strategy to improve the performance and stability of emerging optoelectronics. These scaffolds comprise ordered arrays of nanoconfining spaces, such as cylindrical pores or rectangular grooves, in which semiconductor crystallization occurs. Guiding this area of research is the principle that crystallization within these nanoconfining spaces is fundamentally different than bulk crystallization. First, the restriction of crystal growth in one or two dimensions on the nanoscale results in the preferential orientation of crystals to align their fast growth direction with the unconfined dimension of nanconfining space. Second, the increased surface area-to-volume ratio of nanocrystals compared to bulk crystals shifts the relative Gibbs free energies of polymorphs, resulting in different polymorph transition temperatures.

This tutorial review seeks to explore how crystal orientation selectivity and polymorph transition temperature shifts via nanoconfinement have been used to guide the solution-phase crystallization of small-molecule and polymeric semiconductors into optimized structures for optoelectronic processes. An overview of these classes of solution-processable semiconductors is first provided, along with a description of what constitutes "optimized" structures in common optoelectronic device architectures. A review of recent research progress on the nanoconfined crystallization of solution-processable semiconductors is then summarized, with the impact on overall optoelectronic device performance also discussed. Finally, we conclude with an outlook on future research directions and opportunities in this field.

Solution-Processable Organic Semiconductors

Organic semiconductors that can be dissolved in solvents and deposited as thin films via solution-based methods are generally divided into two main classes: organic small molecules and conjugated polymers. Each of these classes of materials possesses unique attributes and challenges depending on the targeted applications. In this section, we provide a brief overview of these two classes of solution-processable semiconductors.

Small-molecule organic semiconductors

Small-molecule organic semiconductors are carbon-based conjugated compounds in which delocalized π-orbitals across individual molecules allow for charge conduction through crystals in an applied electric field. Unlike doped silicon which transports charge via free carriers, charge transport in organic semiconductors occurs via localized "hopping" via π-orbital overlap between adjacent molecules. The molecular structure, and resulting optoelectronic properties, are tunable via synthetic routes, and an enormous library of small-molecule organic semiconductors has been established over the past few decades. Figure 1 displays four prototypical organic semiconductors and their different packing arrangements in crystals.[1] The charge transport capabilities of these compounds are primarily determined by the magnitude of electron exchange as represented by the charge transfer integral(s), *J*, between adjacent molecules. The largest *J* values are observed along the direction(s) of maximum π-orbital overlap, resulting in charge transport anisotropy along different crystallographic directions.

Of the four compounds displayed in Figure 1, triisopropylsilylethynyl pentacene (TIPS-PEN; Figure 1C) and decyl-substituted dinaphtho[2,3-d:2',3'-d']benzo[1,2-b:4,5-b'] dithiophene (C_{10}-DNBT-NW; Figure 1D) are highly soluble in organic solvents. In addition to a conjugated core with carbon double bonds in which the π-orbitals are delocalized, these molecules incorporate bulky insulating side groups to increase their solubility. The presence of these insulating side groups can significantly affect charge transport by altering the molecular packing arrangement, as well as acting as barriers to charge transport. In triisopropylsilylethynyl pyranthrene crystals, for example, the hole mobility was measured via conductive atomic force microscopy to be two orders of magnitude lower along the [001] direction compared to the [100] direction because charges must hop across layers of bulky silyl groups along the former direction.[2]

The gold standard of organic semiconductor devices is the single crystal due to their near-perfect molecular ordering and absence of grain boundaries that can act as barriers to charge transport. For single-crystal rubrene devices, hole mobilities > 15 cm^2/V-s have been measured,[3] compared to 1 cm^2/V-s for amorphous silicon. To take advantage of the processability of these materials, however, the more practical option is depositing polycrystalline thin films via rapid solution processing methods. In these films, grain boundaries and other defects can act as trap sites, lowering the overall charge mobility in devices compared to those comprising single crystal active layers. Furthermore, because nucleation events occur randomly during solution-phase deposition, controlling crystal orientation to align the fast charge transport direction with the current flow in devices remains a significant challenge. As we

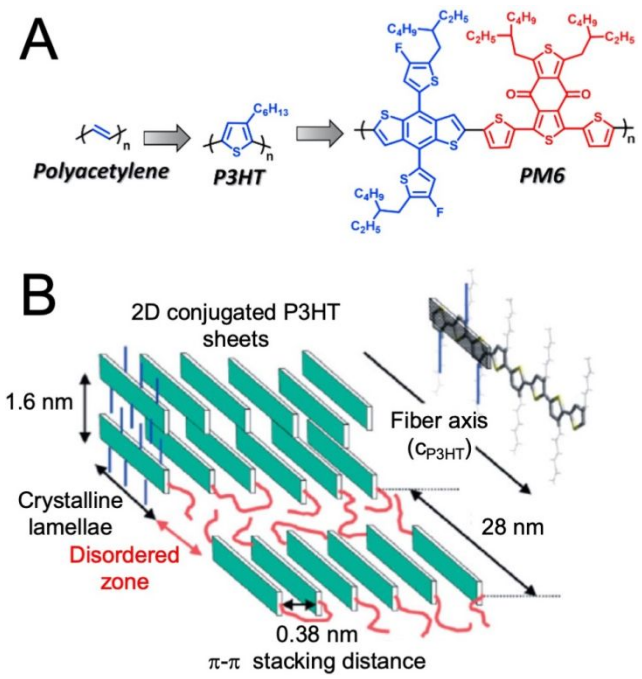

Figure 2. A) Progression of conjugated polymer structures from polyacetylene to poly(3-hexylthiophene) (P3HT) and more complex donor-acceptor polymers, such as PM6. Reproduced with permission from Ref. [4]. Copyright 2020, Elsevier B.V. B) Representative morphology of a semi-crystalline P3HT film, exhibiting crystalline lamellae and disordered regions. Adapted with permission from Ref. [6]. Copyright 2011, Wiley-VCH.

will discuss in this tutorial, nanoconfining crystallization within scaffolds is a strategy to select for specific orientations of small-molecule organic semiconductor crystals in order to optimize their performance in optoelectronic devices.

Conjugated polymers

Conjugated polymers are similar to small-molecule organic semiconductors in that they are carbon-based systems with extended conjugation along the polymer backbone. This class of materials comprises repeat units of conjugated monomers, with tunable optoelectronic properties based on the monomer molecular structure. Conjugated polymer development largely began in the early 1970s, beginning with simple repeat units, such as polyacetylene, progressing to more complex structures of polythiophenes and donor-acceptor polymers that incorporate an electron-donating and electron-accepting monomer in a single repeat unit (Figure 2A).[4] Through the development of novel synthetic routes to target low bandgap polymers with controlled molecular weight distributions, solar cell performance based on conjugated polymers has recently exceeded 16%.[5]

When deposited from solution, conjugated polymers adopt complex morphologies ranging from amorphous to semicrystalline. Figure 2B displays an illustration of crystalline lamellae and disordered domains that form in P3HT films, the workhorse of organic photovoltaics research.[6] Intrachain charge transport along the polymer backbone can be orders of magnitude faster than via interchain hopping through the π-orbital network of crystalline lamellae, which in turn can be order of magnitude faster than charge transport through disordered domains.[1] Because intrachain charge transport is significantly faster than other routes, increasing the number of "tie-chains", or polymer chains that bridge crystalline lamellae, by increasing the polymer chain length is critical to improving overall charge transport through these films. Device performance is thus also strongly dependent on the polymer chain orientation.

Common Device Architectures

For optoelectronic devices, there are generally two main device architectures, one in which the electrodes are co-planar and one in which the electrodes are in a sandwich configuration. In the former case, current flow is parallel to the substrate surface, whereas in the latter case current flow is perpendicular to the substrate surface. In this section, we will briefly review two main device platforms used to test the performance of organic and hybrid semiconductors, the field-effect transistor with a co-planar electrode configuration and the solar cell with a sandwich electrode configuration.

Field-effect transistors with co-planar electrodes

Field-effect transistors (FETs) comprise three electrodes, the drain, source and gate, a gate dielectric, and a semiconducting active layer, with a typical configuration displayed in Figure 3A. The source and drain electrodes can be placed underneath the active layer in a "bottom contact" configuration or on top of the active layer in a "top contact" configuration. The device channel corresponds to the semiconducting active layer that lies between the source and drain electrodes. The gate dielectric is a wide bandgap material, such as SiO_2, that insulates the gate electrode from the source and drain electrodes. Figure 3A displays a "bottom-gate" configuration with the active layer deposited on top of the gate dielectric. The gate dielectric and gate can also be deposited on top of the active layer in a "top-gate" configuration.

In the "off-state" when no gate bias is applied, there is no current flow through the active layer regardless of the applied bias across the source and drain electrodes. In this state, the semiconductor behaves as an insulator. To turn the FET on, a gate bias is applied, creating an electric field. This electric field induces accumulation of majority carriers at the semiconductor/dielectric interface, creating a channel for current flow. If a negative gate bias is applied, holes accumulate at the interface, whereas for a positive applied gate bias, electrons accumulate at the interface. The magnitude of the current flow increases with increasing gate bias until saturation is reached.

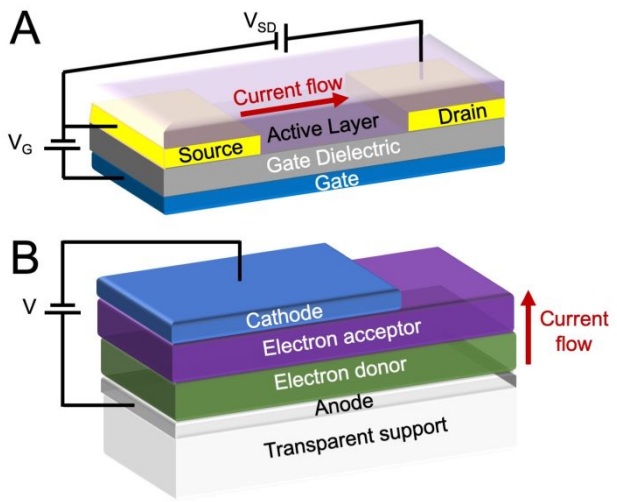

Figure 3. A) Co-planar electrode configuration used for thin film transistors. B) Sandwich electrode configuration used for solar cells. Current flow direction in the devices is indicated by red arrows.

In the co-planar electrode geometry, current flows parallel to the substrate surface through the semiconducting channel. The microstructure of the semiconducting active layer, including the average crystal size and crystal orientation, plays a critical role in determining the overall charge mobility in these devices. In particular, charge transport through semiconducting crystals can exhibit strong anisotropy. As such, the fast charge transport direction of crystals should be aligned parallel to the substrate surface along the direction of current flow to maximize device performance.

Solar cells with sandwich electrodes

Unlike FETs with co-planar electrodes, solar cells and light-emitting diodes use a sandwich electrode architecture with two electrodes, the anode and cathode, sandwiching the semiconducting active layer. Figure 3B displays the typical architecture for a bilayer solar cell in which the active layer comprises an electron donating semiconducting layer and an electron accepting semiconducting layer. These layers have offset bandgaps to promote the dissociation of light-generated excitons, or tightly bond electron-hole pairs. Once separated, holes (electrons) travel through the electron donor (acceptor) to the anode (cathode) for current collection. The anode typically comprises a transparent conductor, such as indium tin oxide or fluorinated tin oxide, coated on a transparent support to allow light to reach the active layer. The cathode is typically a metal with a work function closer to the vacuum level compared to the anode. This offset in work functions between the anode and cathodes creates an internal electric field to direct current flow. As observed from the diagram, current flow in devices with sandwich electrodes occurs perpendicular to the substrate surface. For these devices, it is thus optimal for the fast charge transport direction of semiconducting crystals to also be aligned in the perpendicular direction from the substrate surface.

The Role of Nanoconfinement in Directing Crystallization

There are two main goals in nanoconfining organic semiconductor crystallization during solution processing:

(1) To **control the orientation** of organic semiconductor crystals such that the crystallographic axis exhibiting the largest charge mobility is aligned with the direction of charge transport in the device.
(2) To **select for high mobility polymorphs** of organic semiconductor crystals in order to improve device performance.

Figure 4A displays the principle behind crystal orientation control within nanoconfined spaces. For needlelike crystals confined within cylindrical nanopores, crystals whose long axes are aligned with the long axes of the nanopores can grow larger than misaligned crystals. For sufficiently small pore diameters, misoriented nuclei may not be able to achieve the critical nucleus size needed to induce crystallization.[7] In general terms, the fast growth direction of crystals preferentially align with the unconfined direction of the nanoconfining space. This phenomenon has been observed in many small molecule systems, including glycine,[8] anthranilic acid,[9] and acetaminophen.[10]

Crystal polymorphism can also be controlled within nanoconfined spaces. Polymorphism in crystals is defined as the ability of a compound to adopt different crystal structures. Optoelectronic properties are polymorph-dependent, with small changes to molecular packing arrangements resulting in large changes to the charge transfer integral between organic molecules. The thermodynamically-favored polymorph at a given pressure and temperature is determined by the total Gibbs free energy, G_T, which can be described at the sum of the volume free energy, G_V and surface free energy:[11]

$$G_T = G_V + \left(\frac{\sigma}{\rho}\right)\frac{A}{V} \quad (2)$$

where σ is the energy of the crystal surface per unit area, ρ is the bulk crystal density, A is the mean total surface area and V is the mean volume per crystal. As the size of crystals is reduced, the A/V term correspondingly increases, resulting in an increase in the total Gibbs free energy. Figure 4B displays a comparison

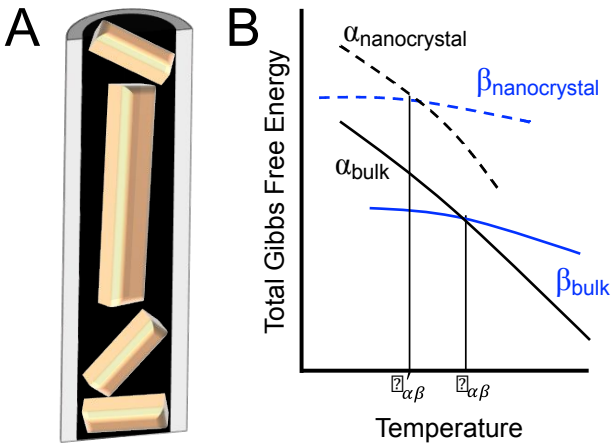

Figure 4. A) Illustration of needlelike crystals with different orientations grown within a cylindrical nanopore. B) Gibbs free energy versus temperature for a representative system in the bulk versus nanocrystalline phase.

of the Gibbs free energy curves versus temperatures for two different polymorphs, labelled α and β, in bulk crystals and nanocrystals with large surface area-to-volume ratios. In this system, the α phase is thermodynamically-favored at high temperatures (i.e has a lower Gibbs free energy) while the β phase is favored at low temperatures. The solid-state phase transition temperature occurs at the point where their Gibbs free energies are equal, labelled as $T_{\alpha\beta}$ and $T'_{\alpha\beta}$ for the bulk and nanocrystal phases, respectively.

Both goals of controlling organic semiconductor crystal orientation and polymorphism via nanoconfined crystallization have been pursued over the past two decades. In the following sections of the tutorial review, we review progress in the field of organic optoelectronics through the use of nanoconfining scaffolds.

Orientation Control via Nanoconfinement

Crystal growth anisotropy in small-molecule semiconductors

Orientation control via nanoconfinement of molecular crystals takes advantage of crystal growth rate anisotropies along different crystallographic directions. To a first approximation, fast crystallographic growth directions of molecular crystals correspond to those along which there are strong intermolecular interactions. Solute molecule attachment to crystal surfaces is the rate limiting step in solution-phase crystal growth, and strong interactions result in high attachment energies to facilitate rapid growth.[12] Crystallographic growth rates are also sensitive to the surrounding environment, such as the presence of molecular additives that preferentially attach to specific crystallographic faces.[13]

In crystals comprising small-molecule organic semiconductors, the crystallographic direction(s) associated with strong intermolecular interactions are those with π-orbital overlap between adjacent molecules. In other words, fast crystallographic growth directions correspond to crystallographic directions characterized by the largest charge transfer integral, *J*. Because *J* is sensitive to the molecular structure and packing motif, small changes in the molecular structure can result in macroscopic changes to the overall crystal morphology. Figure 5 displays the molecular structures and crystals of three anthracene-based cruciforms.[14] As observed from the figure, small changes in the molecular structure resulted in large differences in the crystal morphology. For 9,10-bis(phenyl-2-ylethynyl)anthracene (BPEA) in Figure 5A, needle-like crystals were observed. This compound was found to adopt a herringbone packing motif with π-stacking along the [010] direction and C-H···π interactions between a molecule and its four nearest neighbors. As observed from the SEM image and illustration of the molecular packing, the π-stack direction thus corresponds to the long axis of the needles. For 9,10-bis(naphthalen-2-ylethynyl)anthracene (BNEA), a herringbone motif was also observed (Figure 5B). Compared to BPEA, BNEA exhibited weaker π-π overlap between adjacent anthracene cores and interactions between a molecule and its 10 nearest neighbors via C-H···π interactions. This compound formed two-dimensional ribbon-like crystals, with the fastest growth still occurring along the π-stack, e.g. [010] direction. For 9,10-bis(thiophen-2-ylethynyl)anthracene (BTEA) displayed in Figure 5C, three-dimensional crystals with hexagonal shapes were observed. The molecular packing of BTEA is characterized by the formation of dimers with strong π-π and S···S interactions, but no significant π-π interactions between dimers.

As observed from the above illustrative example, fast crystallographic growth directions are largely determined by the strength of intermolecular interactions. For 1D needlelike crystals and 2D platelike crystals, morphologies commonly observed in small-molecule organic semiconductor systems, the

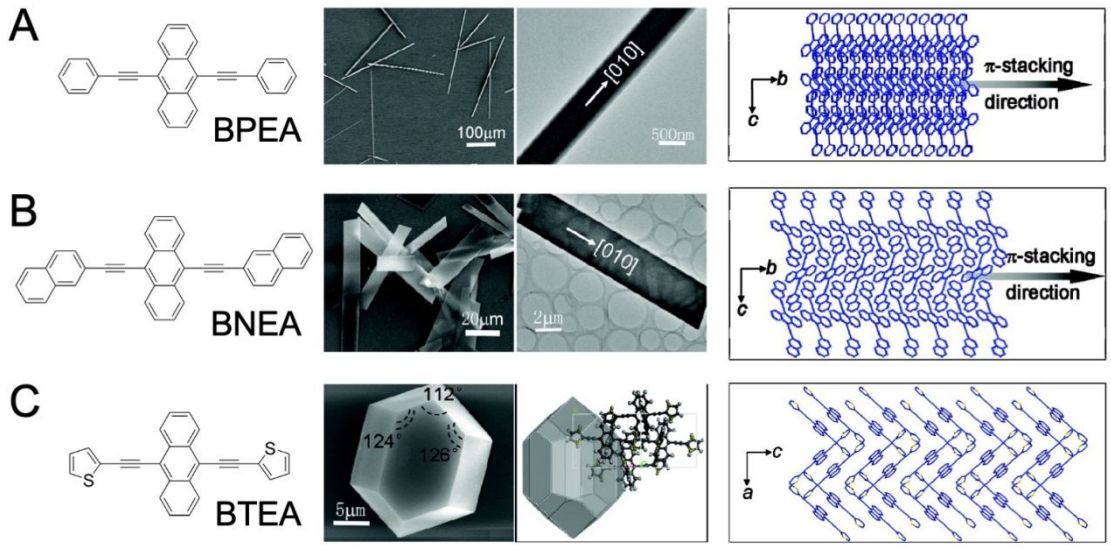

Figure 5. Molecular structures, crystals and illustrations of molecular packing for A) 9,10-Bis(phenyl-2ylethynyl)anthracene, B) 9,10-Bis(naphthalen-2-ylethynyl)anthracene, and C) 9,10-Bis(thiophen-2-ylethynyl)anthracene. Adapted with permission from Ref. 14. Copyright 2009, American Chemical Society.

long axis(es) of the crystals correspond to the direction of maximum π-orbital overlap.[3] In these systems, the long axes of the crystals also represent the direction of fastest charge transport. Much effort has thus focused on aligning the fast crystallographic growth direction with the charge transport direction in devices depending on the device architecture.

Orientation control via nanoconfinement

The relationship between crystal morphology and charge transport in organic semiconductor crystals, i.e. the fast crystallographic growth direction corresponds to the fast charge transport direction, is the underlying principle guiding the use of nanoconfinement to select for specific orientations of small-molecule organic semiconductors. As discussed in a previous section, in the confined spaces on nanostructured scaffolds, crystals tend to orient with their fast growth directions aligned with direction that is unconfined by the scaffold. By designing nanoconfining scaffolds with unconfined directions either parallel or perpendicular to the scaffold surface, it is thus possible to optimize the orientation of organic semiconductor crystals for either co-planar electrode or sandwich electrode devices.

In-plane alignment of small-molecule crystals. For devices with coplanar electrodes, such as transistors, current flow during device operation proceeds parallel to the substrate surface. It is thus advantageous to preferentially align the π-stack direction of organic semiconducting crystals parallel to the substrate surface along the shortest path between the electrodes. To achieve this preferential alignment via nanoconfined crystallization, researchers have explored crystallization of organic semiconductors in grooves etched into substrate surfaces. One of the first reports of confined organic semiconductor crystallization was published by Hwang and co-workers in 2010, who used a liquid-bridge-mediated nanotransfer molding technique to form TIPS-PEN crystalline wires within topographic grooves of polyurethane acrylate and polydimethylsiloxane molds,[15] as displayed in Figure 6A. In this method, organic semiconductor solutions were first solidified within ca. 100 nm grooves of the polymer mold and then transferred to a silicon substrate using a liquid bridge to facilitate the transfer of wires and subsequent mold removal. While crystal orientation was not examined in this work, a later study by the same group confirmed that TIPS-PEN nanowires formed by this method were single-crystalline in nature, with the TIPS-PEN π-stack direction parallel to the groove direction.[16] Similar preferred orientation was observed for single crystalline wires of 8,16-didodecyl-8,16-dihydrobenzo[a]benzo[6,7]indolo[2,3-h]-carbazole (C12-BBICZ) formed by the same method.[17] Figure 6B displays an SEM image of C12-BBICZ wires after transfer and mold removal in which the groove widths in the molds were 90 nm. Selective area electron diffraction and XRD patterns collected on these wires confirmed that they were single-crystalline and oriented with the π-stack direction parallel to the groove direction, as displayed in Figure 6C. Hole mobilities of the C12-BBICZ wires extracted from field-effect transistors were measured to be ~1.5 cm^2/V-s. In these devices, the

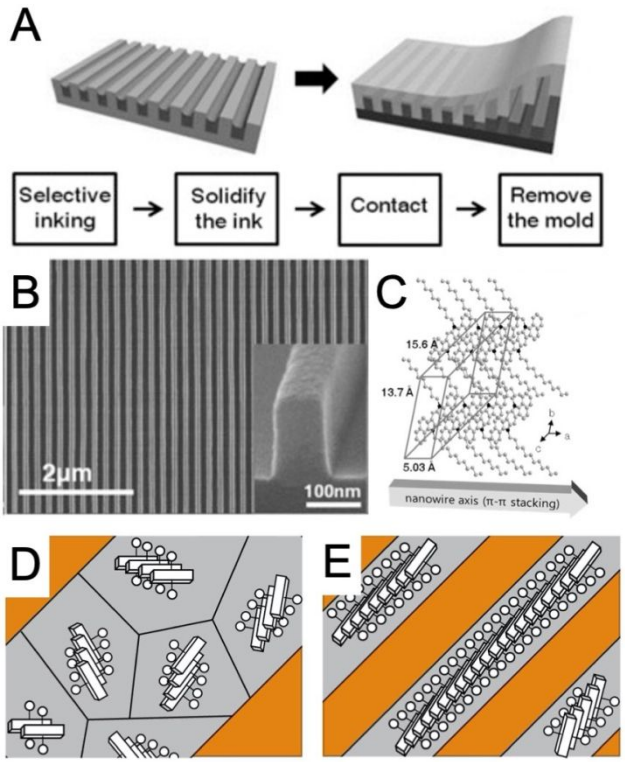

Figure 6. A) Illustration of the liquid-bridge-mediated nanotransfer molding technique to fill polymer molds with organic semiconductor solutions. After organic semiconductor crystallization upon solvent evaporation, the wires were transferred to a substrate and the mold removed. B) SEM image of C12-BBICZ wires (width = 90 nm) after mold removal. C) Illustration of the C12-BBICZ molecular orientation in which the π-stack direction aligned parallel to the long axis of the nanowire. Adapted with permission from Ref. 17. Copyright 2013, Wiley-VCH. D and E) Illustrations of TIPS-PEN crystals within grooves with widths > 20 μm and < 20 μm, respectively. Reproduced with permission from Ref. 20. Copyright 2019, Elsevier.

electrodes were placed such that the nanowires spanned the channel between the electrodes parallel to the direction of current flow.

In a similar approach, Jo and coworkers used PDMS molds in direct contact with silicon substrates to form nanowires of dioctylbenzothienobenzothiophene (C8-BTBT).[18] Capillary forces were used to fill the grooves with organic semiconductor solutions, which were then allowed to solidify prior to mold removal. The Park group subsequently examined the use of capillary force lithography to form TIPS-PEN nanowires in grooves of polymer molds ranging from 50 nm – 100 μm. [19,20] In all of these reports, when the groove width was sufficiently narrow, preferential alignment of the fast growth direction of the crystals with the long axis of the grooves was observed. Figure 6D and E display illustrations of TIPS-PEN crystals within wide channels (e.g. 100 μm) and narrow channels (e.g. 5 μm), respectively.

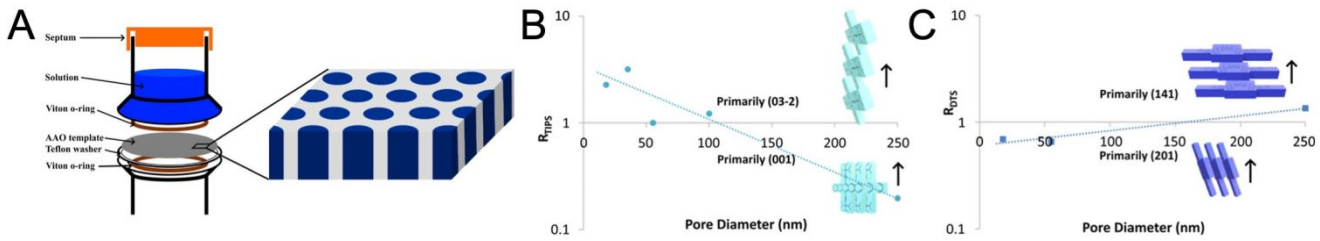

Figure 7. A) Set up to infiltrate AAO templates with organic semiconductor solutions from the top surface while solvent evaporation occurs at the bottom surface. B and C) Ratio of the out-of-plane intensities of the B) $(0\bar{3}2)$ and (001) planes of TIPS-PEN and C) (141) and (201) planes of *p*-DTS(FBTTh$_2$)$_2$ as a function of AAO pore diameter. Adapted with permission from Ref. 36. Copyright 2020, American Chemical Society.

In another variation of confined organic semiconductor crystallization within the grooves of polymer molds, Giri and coworkers introduced shear forces by blade coating solutions into the grooves along the groove direction.[21] Using this approach, uniaxially aligned single-crystalline TIPS-PEN microwires with diameters ranging from 0.5 – 20 μm were formed. Transistors comprising these microwires as the active layer exhibited mobilities as high as 2.7 cm^2/V-s. Kim and coworkers later applied this blade coating approach to confine blends of TIPS-PEN and polystyrene, an insulating polymer, within grooves.[22] Consistent with other reports, an increase in preferential alignment of TIPS-PEN crystals with the π-stack direction parallel to the groove direction with decreasing groove width was observed.

Preferred crystal orientations with the π-stack direction parallel to the groove direction have also been reported for 2,7-didecylbenzothienobenzothiophene (C10-BTBT),[23] triethylsilylethynyl anthradithiophene (TES ADT),[24,25] and a quinoidal oligothiophene derivative[26] processed using similar techniques. In all cases, enhanced charge mobilities in field-effect transistor platforms were reported. These findings indicate that nanoconfined crystallization to induced preferential alignment of small-molecule organic semiconductor crystals is a promising strategy to improve the performance and reproducibility of field-effect transistors and other devices using co-planar electrodes. The ability to direct the growth of single-crystalline nanowires has also enabled the formation of p-n heterojunctions for optoelectronic devices.[27] By sequentially transferring single crystalline nanowires of TIPS-PEN and PCBM grown in polymer molds, for example, Park and coworkers fabricated single-crystal p-n junction arrays exhibiting rectifying behavior.[28]

In-plane orientation of small-molecule organic semiconductors can also be achieved through one-dimensional confinement by limiting the film thickness. Such films, as thin as a single monolayer, are typically deposited via meniscus-guided solution coating.[21,29–32] In this approach, organic semiconductor solutions are deposited via blade coating onto flat substrates. The blade introduces shear forces, which can induce preferential alignment of molecules along the shear direction. By limiting film thicknesses to single monolayers or bilayers, Peng and coworkers achieved millimeter-scale single-crystal domains of 2,9-didecyldinaphtho[2,3-b:2′,3′-f]thieno[3,2-b]thiophene (C10-DNTT).[33] During coating, molecules preferentially aligned with the π-stack direction parallel to the substrate surface. Because of the absence of grain boundaries in these oriented films, high intrinsic mobilities of 12.5 cm^2/V-s were achieved for transistors incorporating these ultrathin films as the active layer. By systematically controlling deposition parameters and solvents, the same group found that key factors governing the formation of large-scale single crystalline domains include the shearing speed, solute concentration, deposition temperature, and solvent boiling point.[34] Furthermore, 1D confinement of organic semiconductors in ultrathin layers can also stabilize high-performance metastable polymorphs, as will be discussed in a following section.

Out-of-plane alignment of small-molecule crystals. The previous examples highlighted the use of nanogrooves lying parallel to the substrate surface to align the π-stack direction of crystals with the charge transport direction of devices with coplanar electrodes. For devices with sandwich electrodes, current flow occurs perpendicular to the substrate surface. Nanoconfining pores should thus be aligned with their unconfined axis perpendicular to the substrate surface. This geometry can be achieved using nanoporous scaffolds, such as anodized aluminum oxide or selectively etched block copolymer templates, exhibiting uniaxially aligned cylindrical pores traversing the scaffold. Pore diameters in these scaffolds can range from the tens to hundreds of nanometers.[35]

Using a solution-based evaporation process to fill AAO templates with organic semiconductor solutions displayed in Figure 7A, Haruk and co-workers recently examined the orientation of TIPS-PEN and 7,7′-[4,4-Bis(2-ethylhexyl)-4H-silolo[3,2-b:4,5-b′]dithiophene-2,6-diyl]bis[6-fluoro-4-(5′-hexyl-[2,2′-bi-thiophen]-5-yl)benzo[c][1,2,5]thiadiazole] (*p*-DTS(FBTTh$_2$)$_2$) crystals embedded in AAO scaffolds as a function

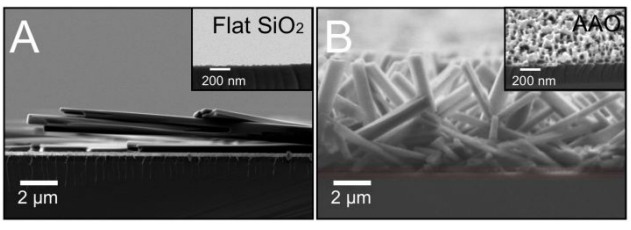

Figure 8. A) Side-view SEM images of TIPS-PY crystals deposited via dip coating onto a A) silicon dioxide substrate and B) silicon dioxide substrate coated with nanoporous AAO (outlined by a red dashed line). Side-view SEM images of the substrates before TIPS-PY deposition are also provided. Reproduced with permission from Ref. 38. Copyright 2019, American Chemical Society.

of pore size.[36] Grazing incidence x-ray diffraction experiments revealed that for pore diameters < 50 nm, TIPS-PEN crystals preferentially aligned with the π-stack direction parallel to the pore direction, as indicated by a larger R value in Figure 7B. This orientation is in line with previous observations of the in-plane orientation of TIPS-PEN crystals in nanogrooves. With increasing pore size, i.e. decreasing confinement, TIPS-PEN crystals increasingly adopted an orientation with the (001) plane parallel to the scaffold surface such that the π-stack direction was perpendicular to the pore direction. Interestingly, nanoconfined *p*-DTS(FBTTH$_2$)$_2$ crystals deposited in the same manner displayed the opposite trend of preferred crystal orientation with increasing pore diameter, as displayed in Figure 7C. These crystals exhibit faster growth along the [201] and π-stack direction. This trend is similar to that reported for *p*-DTS(FBTTH$_2$)$_2$ crystals infiltrated into AAO templates from the melt phase when nucleation occurred within the pores.[37]

One of the factors limiting the use of nanoconfining scaffolds to direct organic semiconductor crystallization for sandwich electrode devices is the difficulty in removing the scaffold. Embedding crystals within nanoporous scaffolds decreases their available surface area for photophysical processes, such as exciton dissociation and recombination. While AAO scaffolds can be etched, crystals lose their preferred orientation during the etching process. To address this issue, our group recently demonstrated the use of nanoconfining scaffolds to form vertical organic semiconductor crystal arrays with large surface.[38] As displayed in Figure 8A, triisopropylsilylethynyl pyranthrene (TIPS-PY) crystals adopt a needlelike morphology when deposited via solution-phase dip coating onto flat SiO_2 substrates. When deposited onto AAO-coated SiO_2 substrates, on the other hand, TIPS-PY crystals grew vertically from the substrate with the π-stack direction perpendicular to the substrate surface (Figure 8B). Critically, crystal growth proceeded above the scaffold surface to form crystal arrays with large available surface areas for photophysical processes. Similar observations were found for perylene crystals deposited from solution onto nanopillar arrays[39] and nanopores.[40]

Preferred orientation in nanoconfined polymers

Orientations in polymer films are typically characterized as "edge-on, "vertical", or "face-on" as displayed in Figure 9 for poly(3-hexylthiophene) (P3HT). In an edge-on orientation, the polymer chain backbones and the π-stack direction are both parallel to the substrate surface. In this orientation, in-plane charge mobility is relatively large, whereas out-of-plane charge mobility is smaller due to the presence of insulating alkyl chains that act as barriers to charge transport. In a face-on orientation, the polymer backbones are also parallel to the substrate surface, but the π-stack direction is perpendicular to the substrate surface. Achieving a face-on orientation of polymer chains can improve charge transport vertically through polymer films, which is advantageous for sandwich electrode device architectures. In the vertical orientation, the polymer chain backbone and π-stack direction are perpendicular and parallel to the substrate surface, respectively. Theoretically, this orientation should exhibit fast charge transport in both the in-plane and out-of-plane directions since charge transport is fastest along the polymer backbone and π-stack direction, but this orientation is not observed in bulk films due to the long, flexible nature of polymer chains that render this orientation unstable. In this section, we will discuss how nanoconfinement can select for different orientations of conjugated polymers.

Conjugated polymer orientation in vertical nanoconfining pores. The most widely studied conjugated polymer for organic solar cells (OSCs) applications is P3HT. When deposited from solution as thin films via spin coating, P3HT forms semicrystalline films in which the crystals adopt an "edge-on" orientation with the conjugated π-planes perpendicular to the surface of the underlying substrate. This orientation is advantageous for devices with coplanar electrodes, such as transistors. For solar cells with sandwich electrodes, on the other hand, a face-on orientation in which the π-stack direction is perpendicular to the substrate is optimal. The first attempt to use nanoconfinement to direct the crystallization of P3HT was by Coakley and co-workers in 2005.[41] In this work, P3HT was infiltrated into AAO templates with average pore diameters ranging from 20 – 120 nm via capillary forces. Using angle-dependent transmission and reflection measurements, it was determined that P3HT chains preferentially aligned along the long axes of nanopores, with the extent of vertical alignment increasing with decreasing pore diameter. This preferential

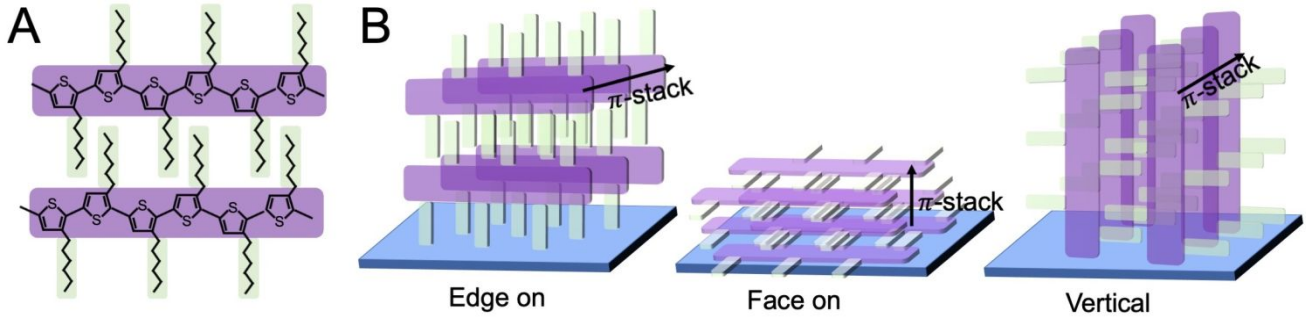

Figure 9. A) P3HT structure, with the conjugated core and insulating side chains highlighted with purple and green, respectively. B) Main orientations of polymer chains with respect to the underlying substrate surface, with the π-stack directions labelled.

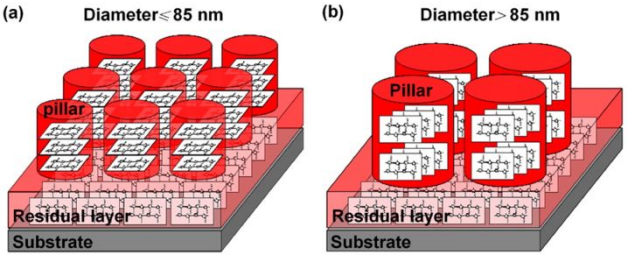

Figure 10. Illustrations of P3HT chain orientation in nanopillars for diameters A) < 85 nm and B) >85 nm. Reproduced with permission from Ref. 44. Copyright 2013, American Chemical Society.

alignment of chains along the vertical direction resulted in up to a 20-fold increase in hole mobility of diodes comprised confined P3HT chains compared to unconfined P3HT films.

In order to measure the effect of nanoconfinement-induced alignment of P3HT on organic solar cell performance, Kim and co-workers placed AAO templates with average pore diameters of 50 nm onto poly(3,4-ethylenedioxythiophene) poly(styrene sulfonate)-coated ITO substrates.[42] Molten P3HT was infiltrated into the cylindrical pores via capillary action under vacuum. In contrast to the work by Coakley and co-workers,[41] X-ray diffraction measurements on the infiltrated AAO templates revealed that P3HT preferentially adopted a face-on orientation with the π-stack direction parallel to the long axis of the confining pore. After removal of the AAO template via chemical etching, C_{60} was deposited thermally evaporated onto the remaining P3HT nanopillars. Solar conversion efficiencies of organic solar cells incorporating P3HT nanopillars/C_{60} bilayers were measured to be 1.12%, compared to only 0.17% for those comprising flat P3HT films. This increase in efficiency was attributed to alignment of the P3HT π-stack direction with the charge transport direction in solar cells, as well as an increase interfacial area between P3HT and C_{60} for exciton dissociation. Such preferred orientation and resulting improvement in light conversion efficiency was also reported by Byun and co-workers for OSCs comprising P3HT nanotubes crystallized in AAO templates.[43]

In 2013, Ding and co-workers examined the threshold for the observation of nanoconfinement-induced preferential orientation of P3HT chains by varying the diameters of AAO scaffold pores from 60 to 130 nm used to imprint P3HT nanopillars.[44] Grazing-incidence wide-angle X-ray diffraction experiments revealed P3HT preferentially aligned with the π-stack direction parallel to the long axis of the nanopillars (e.g. face-on with respect to the underlying substrate surface) for nanopillar diameters < 85 nm, as displayed in Figure 10A. For nanopillar diameters > 85 nm, nanoconfinement-induced preferential orientation was not observed and P3HT chains adopted an edge-on orientation typically observed in unconfined films (Figure 10B). A later study by the same group found improved P3HT/PCBM OSC short-circuit currents for devices comprising P3HT nanopillars with face-on molecular orientations compared to those comprising nanopillars with edge-on molecular orientations.[45] A similar imprinting approach using AAO was also recently applied to n-type polymer poly([N,N′-bis(2-octyldodecyl)naphthalene-1,4,5,8-bis(dicarboximide)-2,6-diyl]-alt-5,5′-(2,2′-bithiophene)) (P(NDI2OD-T2)).[46] In this study, nanostructuring of the PNDI2OD-T2 film to increase the total surface area was found to facilitate exciton dissociation at the interface with a sequentially deposited P3HT layer.

Later on, Xiang and co-workers examined the effect of annealing and melt crystallization on P3HT nanotubes formed in AAO templates with pore diameters of 60 nm and 240 nm.[47] In both templates, P3HT crystals were found to preferentially orient with the π-stack direction parallel to the long axes of the pores. Upon thermal annealing at 200 °C or melting at 240 °C and cooling to room temperature, P3HT nanotubes confined in the larger pore diameters exhibited enhanced crystallinity. For P3HT nanotubes confined in 60 nm pores, on the other hand, annealing and melt crystallization had little effect on the overall crystallinity. These results indicate that structural rearrangement is suppressed with an increasing extent of nanoconfinement.

Comparing the above examples and others,[36,47,48] it is evident that the preferred orientation of P3HT chains within nanoconfining pores depends not only on the extent of nanoconfinement, but also on the processing conditions. Differences in P3HT chain alignment with respect to the cylindrical pores may also be related to different surface energies of the confining templates. P3HT infiltrated into the nanopores of AAO templates treated with low-molecular weight polydimethylsiloxane, for example, were found to adopt

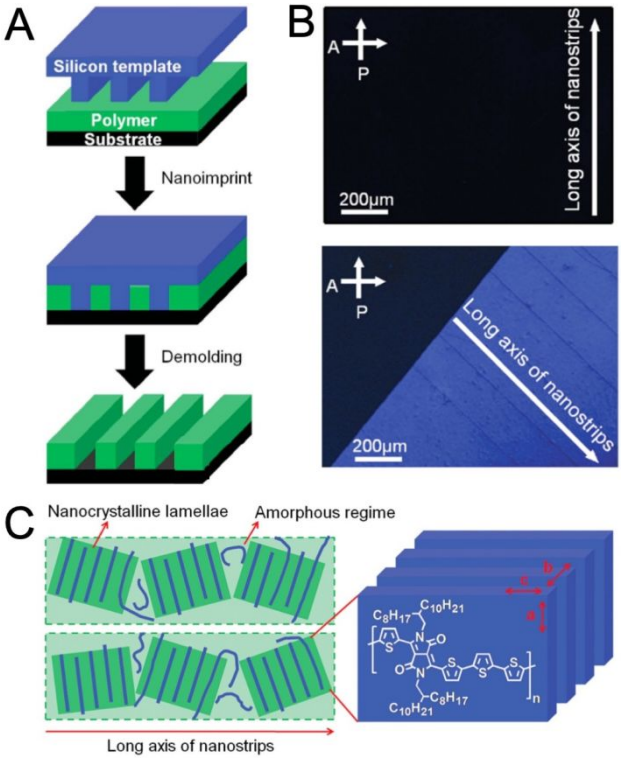

Figure 11. A) Nanoimprint lithography method used to form nanostrips of PDQT. B) Polarized optical microscopy images of PDQT nanostrips at two different orientations with respect to the cross polarizers. C) Illustration of polymer chain orientation with respect to the long axis of the nanostrips. Adapted with permission from Ref. [53]. Copyright 2015, Wiley.

an edge-on orientation with the π-stack direction perpendicular to the long axis of the pores,[49] while a vertical orientation of P3HT chains was reported for P3HT infiltrated into silicon nanopore molds treated with perfluorodecyltrichlorosilane.[50] Collectively, these reports suggest nanoconfined crystallization of organic semiconducting polymers to be a viable strategy to improve solar conversion efficiencies. The use of AAO to form nanostructures in organic solar cell active layers is thus an active area of research.[51]

Conjugated polymer orientation in horizontal grooves. Similar to the experiments on nanoconfined small-molecule semiconductor crystallization discussed in the previous section, the crystallization of conjugated polymers within nanogrooves lying parallel the substrate surface has also been explored. In 2014, for example, Johnston and co-workers confined P3HT/PCBM nanocomposites in silicon gratings with widths of 175 and 47 nm.[52] GIXD patterns on the samples revealed that the (100) diffraction peak exhibited strong intensity at all azimuthal angles for P3HT/PBCM confined in 175 nm-wide gratings, indicating a broad distribution of P3HT crystallite orientations. For P3HT/PCBM confined in gratings with widths of 47 nm, on the other hand, strong preferred orientation of the (100) plane either parallel to the grating direction, indicating that P3HT adopted a primarily face-on orientation in the nanogratings. For pure P3HT crystallized in grooves with larger widths of 5 and 10 μm, on the other hand, Han and co-workers observed P3HT to adopted an edge on orientation.[48] In these samples, P3HT aligned with the π stack direction perpendicular and parallel to the grating direction for 5 μm and 10 μm grooves, respectively. The authors attributed the observed preferred orientations to hydrodynamic effects caused by solvent diffusion into the PDMS mold. In the same report, P(NDI2OD-T2) deposited within the microgrooves in the same manner were found to align in a face-on orientation with the long axis of the polymer chains parallel to the groove direction for both 5 and 10 μm grooves.

Using a nanoimprint lithography method displayed in Figure 11A to form polymer nanowires using a silicon template, Wei and co-workers examined the role of nanoconfinement on the crystallization of a diketopyrrolopyrrole-based polymer, poly[2,5-bis(2-octyldodecyl) pyrrolo-[3,4-c]pyrrole-1,4(2H,5H)-dione-alt-2,2':5',2'':5'',2'''- quaterthiophene] (PDQT).[53] Polarized optical microscopy images of PDQT nanostrips displayed in Figure 11B revealed uniaxially aligned crystals, as evidenced by the uniform light transmission or lack of light transmission depending on the orientation of the nanostrips with respect to the cross polarizers. GIXD was used to determine that PDQT preferentially crystallized with the π-stacking direction parallel to the long axis of the nanostrips, as illustrated in Figure 11C, with more pronounced preferred orientation for strip widths of 160 nm compared to 200 – 280 nm. FETs using these nanostrips as the semiconducting active layer exhibited charge mobilities of 0.08 ± 0.02 cm^2/V-s, compared to 0.004 ± 0.001 cm^2/V-s for unpatterned reference samples. This improvement in mobility was attributed to the alignment of the π-stacking direction with the direction of current flow in the PDQT nanostrips. Similar enhancement in conjugated polymer chain orientation when confined within nanogrooves was also observed in liquid crystalline polymer poly(9,9-dioctylfluorene).[54]

Polymorph Control via Nanoconfinement

In addition to guiding the orientation of organic semiconductor crystals, nanoconfinement can also be used to select for metastable polymorphs of crystals. For metastable polymorphs with larger transfer integrals compared to the thermodynamically stable polymorph, significant increases in charge mobilities have been observed. In this section, we review work examining polymorph control via nanoconfined crystallization and the performance of these polymorphs in optoelectronic devices.

Effect of intermolecular coupling on charge carrier transport

In the charge hopping conduction of organic semiconductors, charge carriers are expected to be localized over a single molecule unit due to strong electron-phonon coupling and trap sites.[55,56] The charge transfer rate, k, can be expressed by the following equation:[57]

$$k = (4\pi^2/h)t^2 (4\pi\lambda RT)^{-0.5} \exp(-\lambda/4RT) \quad (3)$$

where h is Planck's constant, t is the transfer integral, λ is the reorganization energy, R is the distance between molecular centers, and T is the temperature. As observed from the equation, large t values and small λ values are favorable for large charge transfer rates. The transfer integral, t, describes the electronic coupling between two interacting chain, while the reorganization energy, λ, accounts for internal and external contributions. External

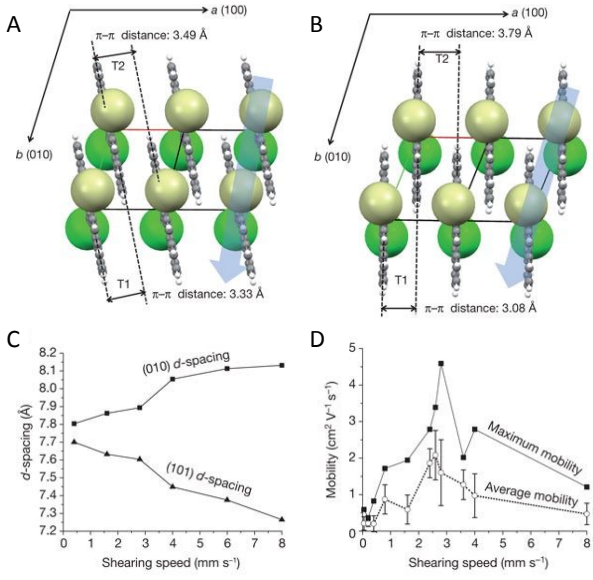

Figure 12. A) Illustrations of molecular packing structure of (a) unstrained and (b) strained thin film, and (c) *d*-spacing and (d) charge carrier mobility as a function of shearing speed, strain for TIPS-pentacene thin films. Adapted with permission from Ref. [61]. Copyright 2011, Nature Publishing Group.

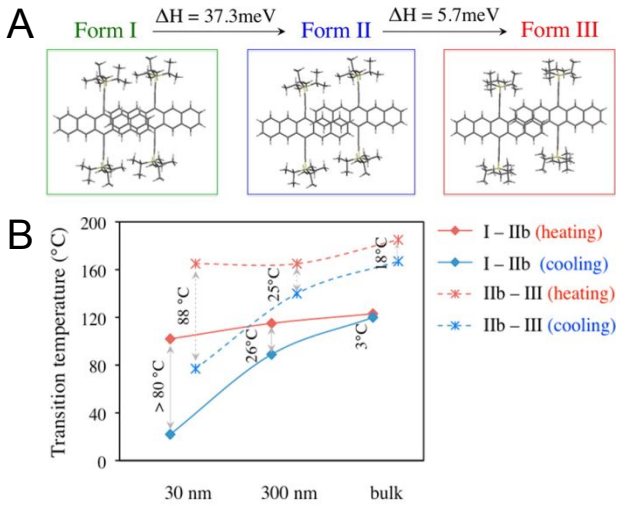

Figure 13. A) Molecular packing in three main polymorphs of TIPS-PEN observed in thin films. B) Transition temperature versus film thickness of TIPS-PEN polymorphs. Adapted with permission from Ref. [69]. Copyright 2014, American Chemical Society.

contributions are associated with changes in the surrounding media accompanying the charge transfer, while internal contributions originate from molecular deformations upon charging. The latter are sensitive to the extent and nature of intermolecular interactions, the molecular rigidity, and the conjugation length, among others.

Because of the strong dependence of charge carrier mobilities on *t*, many experimental and theoretical studies have focused on developing strategies to increase *t* values in organic semiconducting systems. Decreasing π-π stacking distances and altering tilt angle of molecules, for example, can significantly increase transfer integrals by increasing the extent of intermolecular interactions.[58] The displacement of molecules along both long and short axes with respect to adjacent molecules can also influence *t*. For hole transport in tetracene crystals, for example, *t* increases when the molecules along both the long and short axes exhibit either bonding or antibonding interactions between the π-orbitals. If a cancellation of bonding and antibonding interactions occurs, on the other hand, *t* decreases.[57,59,60] Both the extent of π-orbital overlaps and cofacial overlaps between molecules need to be optimized to achieve fast charge transport.

Increasing *t* values can be achieved through controlling the polymorphism, or molecular packing, of organic semiconductor crystals. While one polymorph may be thermodynamically stable in the bulk phase, metastable polymorphs can also form under different processing conditions. Because of the sensitivity of *t* to the molecular packing details, these polymorphs can exhibit significantly different charge mobilities compared to the bulk phase.[61,62] Giri and coworkers, for example, found that solution shearing during the deposition of TIPS-PEN films resulted in a decrease of the π-π stacking distance along the (010) axis of TIPS-PEN crystals from 3.33 Å to as small as 3.08 Å, as displayed in Figure 12.[61] This sub-angstrom decrease in the π-π stacking distance increased the electronic coupling between adjacent molecules, resulting in hole mobilities as high as 4.6 $cm^2 V^{-1} s^{-1}$, nearly six times higher than that of unstrained films . In another study, Kim and coworkers have demonstrated a 5.5 order of magnitude improvement in hole mobility in metastable polymorphs of single-crystalline 2,7-dioctyl[1] benzothieno[3,2-b][1]benzothiophene rods.[63] Such a large modulation in hole mobility can be understood from the orbital interaction between monomers as a function of the molecular tilt (θ_a) ranging from 15° to −15°. These experiments and others highlight the concept that charge mobilities in organic semiconductor systems are sensitive to polymorphism. Developing methods to form metastable polymorphs with enhanced charge transfer integrals compared to the bulk phase is thus a promising strategy to improve charge carrier mobilities in organic semiconductor thin films.

Metastable polymorph stabilization via nanoconfinement

Stabilizing metastable polymorphs of organic semiconductors has been challenging because their intermolecular interactions are characterized by weak van der Waals forces and electrostatic interactions, leading to low kinetic barriers to solid–solid transformations. Nanoconfining organic semiconductors presents a promising strategy to overcome the inherent limitations of stabilizing high-mobility metastable polymorphs.[7,10,19,64] As described earlier, the relative stability of polymorphs is dependent on the crystal size. As the crystal size decreases, the contribution from the thermodynamically unfavorable surface free energy becomes increasingly more significant compared to the thermodynamically favorable volume free energy. At small crystal sizes, polymorphs that are metastable in the bulk phase can become the thermodynamically stable phase.[65,66] Confinement of crystals within scaffolds can further suppress phase transformations between polymorphs by restricting molecular rearrangement.

1D confinement. For emerging optoelectronic device applications, active layer thicknesses are generally a few hundred nanometers or smaller. As film thicknesses decrease to the sub-hundred nanometer range, confinement effects can become significant. “Thin film” polymorphs of organic semiconductors have been reported for pentacene and pentacene derivatives, hexabenzocoronene derivatives, and α-sexithiophene, among others.[67,68] Among solution-processed organic semiconductors, the formation of metastable

polymorphs in thin films has been observed in a number of systems, including TIPS-PEN,[69] TES-ADT,[70] and dihexyl-terthiophene.[71] In addition to nanoconfinement of molecules into thin films, crystallization kinetics can play an important role in forming metastable polymorphs.[71]

In 2014, Diao and coworkers systematically characterized the formation of five different polymorphs of TIPS-PEN and a metastable polymorph [1]benzothieno[3,2-*b*][1]1benzothiopene (BTBT) under 1D nanoconfinement.[69] Using a flow-enhanced deposition method in which solutions are sheared using a blade patterned with micropillars,[62] films with thicknesses of 30 – 300 nm were deposited onto SiO_2 substrates. Figure 13A displays the molecular packing of TIPS-PEN molecules in the three main polymorphs identified, Form I, II and III. The relative stabilities of these phases were found to depend strongly on the film thickness. Figure 13B displays the polymorph transition temperatures as function of film thickness. As observed from the figure, the I-IIb transition shifted from 3°C in the bulk to 80°C in 30 nm-thick films. Hole mobilities measured using thin-film transistor platforms were measured to be 2.4, 8.1, and 0.0058 cm^2/V-s for Forms I, II and III, respectively, demonstrating the critical role of polymorphism in dictating device performance.

Similarly, Burnett and coworkers discovered a thin-film phase of solution-processed N-octyldiisopropylsilyl acetylene bistetracene (BT).[72] When first spun cast from chloroform onto Si substrates, BT was found to adopt a metastable polymorph with a slipped 1D π-stacking motif. A polymorph transition to the bulk phase could be induced by exposing the thin film to solvent vapor. This transition led to a three order of magnitude increase in charge mobility in the bulk phase polymorph, exhibiting 2D brick-layer π-stacking, compared to the thin film polymorph. Temperature-dependent mobility measurements revealed different charge transport mechanisms through the two polymorphs. In the thin film phase, charge hopping was found to be thermally activated, while the bulk phase exhibited intrinsic transport dominated by phonon scattering.

2D confinement. Control over organic semiconductor polymorphism in 2D nanoconfining geometries, such as cylindrical nanopores or rectangular grooves, has been demonstrated for a number of different systems. In 2014, Martin and co-workers demonstrated both preferential orientation and polymorph selectivity of melt-processed poly(3-hexylthiophene) (P3HT) crystals nanoconfined within AAO templates.[73] For pore sizes ranging from 120 – 250 nm, P3HT crystals were found to orient with the π-stack direction parallel to the long axis of pores. For pore sizes of 15, 25, and 50 nm, on the other hand, the π-stack direction of crystals was found to predominantly align perpendicular to the nanowire long axis. Crystals within 15 and 25 nm-diameter pores were further found to preferentially adopt a metastable polymorph, labeled form II. In the bulk phase, form II transitions to the stable form I phase around 50 °C. In nanoconfined pores, on the other hand, form II was stable up to temperatures as high as 210 °C. For form II crystals, the aliphatic chains are interlocked, leading to smaller spacing along the *a* axis compared to form I. These

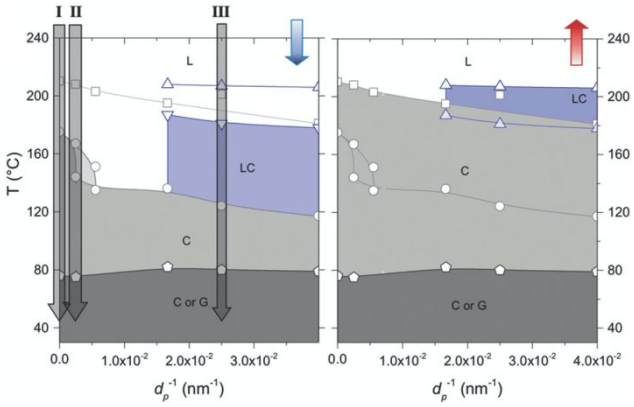

Figure 14. Phase diagram for *p*-DTS(FBTTh$_2$)$_2$ as a function of the extent of nanoconfinement and temperature during cooling (left) and heating (right). Adapted with permission from Ref. [74]. Copyright 2018, Wiley.

observations on shifted polymorph transition temperatures are consistent with a shift of the relative Gibbs free energies of the nanocrystals compared to the bulk. Molecular strain may also be introduced at the walls of the confining AAO scaffold.

Following this work, Martin and coworkers recently demonstrated the influence of nanoconfinement on the polymorphism of small-molecule organic semiconductor *p*-DTS(FBTTh$_2$)$_2$ crystallized within cylindrical nanopores of AAO scaffolds.[74] This compound, which exhibits rich phase behavior, was infiltrated into nanopores by wetting the AAO templates with molten *p*-DTS(FBTTh$_2$)$_2$ at 240 °C, and then samples were quenched directly to the room temperature. Temperature-dependent grazing incidence x-ray diffraction experiments revealed the formation of a liquid crystalline phase during cooling for *p*-DTS(FBTTh$_2$)$_2$ confined within 40 nm-diameter (or smaller) pores. This phase was not observed for samples cooled from the bulk or within 400 nm-diameter pores, as indicated by the phase diagram in Figure 14. The authors hypothesized that nanoconfining *p*-DTS(FBTTh$_2$)$_2$ within 40 nm-diameter pores shifted the relative Gibbs free energies of the different phases sufficiently to stabilize the liquid crystalline phase over a broad range of temperatures. At room temperature, *p*-DTS(FBTTh$_2$)$_2$ adopted the same bulk crystal structure regardless of the extent of confinement. As observed in other nanoconfined systems described in the previous section, nanoconfinement induced preferential orientation of *p*-DTS(FBTTh$_2$)$_2$ crystals. Interestingly, all nanoconfined p-DTS(FBTTh$_2$)$_2$ samples exhibited higher photoconductivity compared to bulk samples, although the mechanism for this improvement remains unclear.

The use of lithography to form nanoconfining grooves has also been employed as a strategy to stabilize metastable polymorphs of organic semiconductors. In 2016, Kim and coworkers examined the confinement of TIPS-PEN in nanogrooves defined by e-beam lithography.[19] Compared to the bulk phase, nanoconfined crystals exhibited a preferential orientation in nanogrooves, as discussed in a previous section. It was further discovered that nanoconfined crystals exhibited a closer π-π stacking distance compared to bulk TIPS-PEN crystals. Transistors comprising metastable TIPS-PEN crystals

exhibited maximum hole carrier mobilities of 9.71 $cm^2 V^{-1} s^{-1}$, comparable to the highest value reported among TIPS-PEN based OTFTs. Accordingly, to maximize performance, many studies have focused on discovering new polymorphs and developing methods to preferientially align them with the current flow direction of devices. Still the mobilities of these metastable thin film polymorphs continue to lag behind bulk single crystals ue ot the presence of grain boundaries that can impede charge transport. For example, highly ordered thin pentacene films can exhibit mobilities higher than 1 $cm^2 V^{-1} s^{-1}$,[75] whereas the mobility of a pentacene single crystal is as high as 35 $cm^2 V^{-1} s^{-1}$ at room temperature.[76]

Gentili and coworkers recently examined the use of a temporary scaffold to confine organic semiconductor thieno(bis)imide end-functionalized terthiophene during solution-phase crystallization.[64] In this process, the terthiophene derivative and *p*-dichlorobenzene were co-dissolved in either chloroform or toluene and the solution was drop-cast onto a substrate. During solvent evaporation, the terthiophene derivative crystallized within a *p*-dichlorobenzene crystalline matrix exhibiting mesoscopic cavities. p-dichlorobenzene was then sublimed from the film, leaving behind organic semiconductor crystals. Interestingly, these crystals adopted the α-polymorph when crystallized in the presence of *p*-dichlorobenzene. In the absence of *p*-dichlorobenzene, on the other hand, a mixture of α- and β-phase crystals formed. This suppression of β-phase crystals in the presence of *p*-dichlorobenzene was attributed to the nanoconfinement of terthiophene derivative crystals between p-dichlorobenzene crystals, which favored α-phase formation. Promisingly, this method to use a temporary scaffold to confine crystallization does not rely on energy-intensive methods for patterning nanoconfining scaffolds. Furthermore, the unconfined organic semiconductor crystals after template sublimation exhibit high surface areas for optoelectronic processes.

Conclusions and outlook

As discussed in this tutorial review, nanoconfining solution-phase crystallization can overcome kinetic limitations of rapid solution processing that result in heterogeneous films with complex microstructures and thermodynamic limitations that favor low-performance polymorphs in the bulk. This field of research focuses on imposing ordering on solution-processed semiconducting films by restricting crystallization in arrays of nanoconfining spaces, such as cylindrical nanopores and rectangular nanogrooves. In this manner, crystal orientations and polymorphs can be prescribed through judicious scaffold design *a priori* while retaining compatibility with high throughput, solution-phase deposition of semiconducting materials.

On a fundamental level, nanoconfining crystallization has provided insights into the solution-phase assembly behavior and orientation- and polymorph-dependent optoelectronic properties of solution-processable semiconductors. Looking forward towards the commercialization of these materials, innovation in scaffold materials will accelerate the use of nanoconfinement as a general strategy to optimize film microstructures. In the examples highlighted in this review, the most common scaffolds employed were anodized aluminum oxide and silicon dioxide, both of which are large bandgap insulators. The presence of these scaffolds necessarily reduces the overall active layer volume, thereby decreasing current flow per unit area of the device compared to devices without nanoconfining scaffolds. In some cases, the scaffolds were removable, for example when polymer molds were used, but the removal process itself can be energy- and time-intensive. The development of solution-processed nanoconfining scaffolds that can participate in optoelectronic processes, such as selectively-etched block copolymer films in which the non-etched block comprises a conjugated polymer, will facilitate high-throughput production of these films.

Myriad opportunities in the exploration of molecule-scaffold interactions, as well as the role of pore geometry and scaffold design on crystallization outcomes also remain. The vast majority of studies thus far have focused on the use of uniaxially aligned grooves or nanopores to confine organic semiconductor crystallization during solution-phase deposition. The ability to grow single crystalline nanowires along arbitrary shapes and directions could enable the fabrication of more complex integrated circuits. Furthermore, scaffold geometries can play an important role in dictating crystal polymorphism[77] and orientation[40,78] via graphoepitaxy. Coupled with chemical treatments to tune the scaffold surface energy, judicious scaffold design may enable the a priori determination of crystal locations, orientations, polymorphs and sizes. To take full advantage of the processability of soluble organic semiconductors, these scaffolds should be compatible with continuous processing methods.

Overall, progress in the field of nanoconfined emerging optoelectronics has evolved through an Edisonian, trial-and-error approach, with processing conditions and confinement parameters optimized individually for different organic semiconductor systems. Given the enormous library of solution-processable semiconductors developed over the past few decades, theoretical methods to predict polymorph and orientations based on the extent of confinement based on fundamental principles will undoubtedly accelerate advances in this field. In particular, predicting high-performance polymorphs and identifying the extent of nanoconfinement needed to stabilize them will guide the design of nanoconfining scaffolds based for different organic semiconductor chemical structures. We thus expect advances in scaffold materials and designs, supported by a deeper understanding of the fundamental factors governing nanoconfined crystallization to dictate orientation and polymorph outcomes, will advance the field of emerging optoelectronics towards large-scale manufacturing of high-performance devices in the future.

Conflicts of interest

There are no conflicts to declare.

Acknowledgements

The authors acknowledge support from the National Science Foundation under Award No. CMMI-AM-1846178. The authors are also grateful for support from the PSEG Foundation to advance energy innovation at Stevens Institute of Technology.

References

1 S. Fratini, M. Nikolka, A. Salleo, G. Schweicher and H. Sirringhaus, *Nat. Mater.*, 2020, **19**, 491–502.

2 X. Bai, K. Zong, J. Ly, J. S. Mehta, M. Hand, K. Molnar, S. Lee, B. Kahr, J. M. Mativetsky, A. Briseno and S. S. Lee, *Chem. Mater.*, 2017, **29**, 7571–7578.

3 C. Wang, H. Dong, L. Jiang and W. Hu, *Chem. Soc. Rev.*, 2018, 47, 422–500.

4 R. M. Pankow and B. C. Thompson, *Polymer (Guildf).*, 2020, **207**, 122874.

5 NREL, *Best Res. Effic. Chart | Photovolt. Res. | NREL*, 2020, https://www.nrel.gov/pv/cell-efficiency.html.

6 M. Brinkmann, *J. Polym. Sci. Part B Polym. Phys.*, 2011, 49, 1218–1233.

7 B. D. Hamilton, J.-M. Ha, M. A. Hillmyer and M. D. Ward, *Acc. Chem. Res.*, 2012, **45**, 414–423.

8 B. D. Hamilton, M. A. Hillmyer and M. D. Ward, *Cryst. Growth Des.*, 2008, **8**, 3368–3375.

9 J. Ha, J. H. Wolf, M. A. Hillmyer and M. D. Ward, 2004, 3382–3383.

10 G. Graubner, G. T. Rengarajan, N. Anders, N. Sonnenberger, D. Enke, M. Beiner and M. Steinhart, *Cryst. Growth Des.*, 2014, **14**, 78–86.

11 G. T. Rengarajan, D. Enke, M. Steinhart and M. Beiner, *Phys. Chem. Chem. Phys.*, 2011, **13**, 21367–21374.

12 P. Dandekar, Z. B. Kuvadia and M. F. Doherty, *Annu. Rev. Mater. Res.*, 2013, **43**, 359–386.

13 A. G. Shtukenberg, S. S. Lee, B. Kahr and M. D. Ward, *Annu. Rev. Chem. Biomol. Eng.*, 2014, **5**, 77–96.

14 C. Wang, Y. Liu, Z. Ji, E. Wang, R. Li, H. Jiang, Q. Tang, H. Li and W. Hu, *Chem. Mater.*, 2009, **21**, 2840–2845.

15 J. K. Hwang, S. Cho, J. M. Dang, E. B. Kwak, K. Song, J. Moon and M. M. Sung, *Nat. Nanotechnol.*, 2010, **5**, 742–748.

16 K. S. Park, B. Cho, J. Baek, J. K. Hwang, H. Lee and M. M. Sung, *Adv. Funct. Mater.*, 2013, **23**, n/a-n/a.

17 K. S. Park, S. M. Salunkhe, I. Lim, C.-G. Cho, S.-H. Han and M. M. Sung, *Adv. Mater.*, 2013, **25**, 3351–3356.

18 P. S. Jo, A. Vailionis, Y. M. Park and A. Salleo, *Adv. Mater.*, 2012, **24**, 3269–3274.

19 K. Kim, Y. Rho, Y. Kim, S. H. Kim, S. G. Hahm and C. E. Park, *Adv. Mater.*, 2016, **28**, 3209–3215.

20 H. J. Kwon, K. Kim, T. K. An, S. H. Kim and C. E. Park, *J. Ind. Eng. Chem.*, 2019, **75**, 187–193.

21 G. Giri, S. Park, M. Vosgueritchian, M. M. Shulaker and Z. Bao, *Adv. Mater.*, 2014, **26**, 487–493.

22 K. Kim, J. Hong, S. G. Hahm, Y. Rho, T. K. An, S. H. Kim and C. E. Park, *ACS Appl. Mater. Interfaces*, 2019, **11**, 13481–13490.

23 A. Kim, K. S. Jang, J. Kim, J. C. Won, M. H. Yi, H. Kim, D. K. Yoon, T. J. Shin, M. H. Lee, J. W. Ka and Y. H. Kim, *Adv. Mater.*, 2013, **25**, 6219–6225.

24 K. Kim, M. Jang, M. Lee, T. K. An, J. E. Anthony, S. H. Kim, H. Yang and C. E. Park, *J. Mater. Chem. C*, 2016, **4**, 6996–7003.

25 K. V. Nguyen, J. H. Lee, S. C. Lee, G. M. Ku and W. H. Lee, *Org. Electron.*, 2017, **41**, 107–113.

26 S. Watanabe, T. Fujita, J.-C. Ribierre, K. Takaishi, T. Muto, C. Adachi, M. Uchiyama, T. Aoyama and M. Matsumoto, *ACS Appl. Mater. Interfaces*, 2016, **8**, 17574–17582.

27 Q. Li, S. Ding, W. Zhu, L. Feng, H. Dong and W. Hu, *J. Mater. Chem. C*, 2016, 4, 9388–9398.

28 K. S. Park, K. S. Lee, C. M. Kang, J. Baek, K. S. Han, C. Lee, Y. E. Koo Lee, Y. Kang and M. M. Sung, *Nano Lett.*, 2015, **15**, 289–293.

29 G. Giri, E. Verploegen, S. C. B. Mannsfeld, S. Atahan-Evrenk, D. H. Kim, S. Y. Lee, H. A. Becerril, A. Aspuru-Guzik, M. F. Toney and Z. Bao, *Nature*, 2011, **480**, 504–508.

30 Y. Diao, B. C.-K. Tee, G. Giri, J. Xu, D. H. Kim, H. a Becerril, R. M. Stoltenberg, T. H. Lee, G. Xue, S. C. B. Mannsfeld and Z. Bao, *Nat. Mater.*, 2013, **12**, 665–71.

31 H. B. Akkerman, A. C. Chang, E. Verploegen, C. J. Bettinger, M. F. Toney and Z. Bao, *Org. Electron.*, 2012, **13**, 235–243.

32 R. Janneck, F. Vercesi, P. Heremans, J. Genoe and C. Rolin, *Adv. Mater.*, 2016, **28**, 8007–8013.

33 B. Peng, K. Cao, A. Ho, Y. Lau, M. Chen, Y. Lu and P. K. L. Chan, *Adv. Mater.*, 2020, **32**, 2002281.

34 M. Chen, B. Peng, S. Huang, P. Kwok and L. Chan, *Adv. Funct. Mater.*, 2020, **1905963**, 1905963.

35 X. Kong, K. Zong and S. S. Lee, *Chem. Mater.*, 2019, **31**, 4953–4970.

36 A. M. Haruk, C. Z. Leng, P. S. Fernando, D.-M. Smilgies, Y.-L. Loo and J. M. Mativetsky, *J. Phys. Chem. C*, 2020, **14**, 22799–22807.

37 J. Martín, M. Dyson, O. G. Reid, R. Li, A. Nogales, D. M. Smilgies, C. Silva, G. Rumbles, A. Amassian and N. Stingelin, *Adv. Electron. Mater.*, 2018, **4**, 1700308.

38 K. Zong, Y. Ma, K. Shayan, J. Ly, E. Renjilian, C. Hu, S. Strauf, A. Briseno and S. S. Lee, *Cryst. Growth Des.*, 2019, **19**, 3461.

39 K. Zong, K. M. Asawa, A. Circelli, N. Sparta, C. Choi and S. S. Lee, *ACS Mater. Lett.*, 2020, **2**, 721–726.

40 A. Alaei, K. Zong, K. Asawa, T.-M. Chou, A. L. Briseño, C.-H. Choi and S. S. Lee, *Soft Matter*, 2021, **17**, 3603–3608.

41 K. M. Coakley, B. S. Srinivasan, J. M. Ziebarth, C. Goh, Y. Liu and M. D. McGehee, *Adv. Funct. Mater.*, 2005, **15**, 1927–1932.

42 J. S. Kim, Y. Park, D. Y. Lee, J. H. Lee, J. H. Park, J. K. Kim and K. Cho, *Adv. Funct. Mater.*, 2010, **20**, 540–545.

43 J. Byun, Y. Kim, G. Jeon and J. K. Kim, *Macromolecules*, 2011, **44**, 8558–8562.

44 G. Ding, Y. Wu, Y. Weng, W. Zhang and Z. Hu, *Macromolecules*, 2013, **46**, 8638–8643.

45 G. Ding, C. Li, X. Li, Y. Wu, J. Liu, Y. Li, Z. Hu and Y. Li, *Nanoscale*, 2015, **7**, 11024–11032.

46 T. Pfadler, M. Coric, C. M. Palumbiny, A. C. Jakowetz, K.-P. Strunk, J. A. Dorman, P. Ehrenreich, C. Wang, A. Hexemer, R.-Q. Png, P. K. H. Ho, P. Müller-Buschbaum, J. Weickert

and L. Schmidt-Mende, *ACS Nano*, 2014, **8**, 12397–12409.
47 W. Xiang, X. Sun, Z. Ren, J. Zhang, H. Li and S. Yan, *J. Mater. Chem. C*, 2017, **5**, 8315–8322.
48 M. J. Han, J. Kim, B. Kim, S. M. Park, H. Ahn, T. J. Shin, B. Kim, H. Kim and D. K. Yoon, *ACS Nano*, 2020, **14**, 12951–12961.
49 D. Chen, W. Zhao and T. P. Russell, *ACS Nano*, 2012, **6**, 1479–1485.
50 A. Mukti, T. Krutarth and W. Hu, *ACS Nano*, 2009, **3**, 3085–3090.
51 A. J. Goszczak and P. P. Cielecki, *Curent Nanosci.*, 2019, **15**, 64–75.
52 D. E. Johnston, K. G. Yager, H. Hlaing, X. Lu, B. M. Ocko and C. T. Black, *ACS Nano*, 2014, **8**, 243–249.
53 S. Wei, Y. Zhang, J. Liu, X. Li, Y. Wu, H. Wei, Y. Weng, X. Gao, Y. Li, S.-D. Wang and Z. Hu, *Adv. Mater. Interfaces*, 2015, **2**, 1500153.
54 S. Oh, R. Hayakawa, T. Chikyow and Y. Wakayama, *Appl. Phys. Lett.*, 2015, **106**, 243301.
55 J. L. Bredas and G. B. Street, *Acc. Chem. Res.*, 1985, **18**, 309–315.
56 A. J. Heeger, S. Kivelson, J. R. Schrieffer and W. P. Su, *Rev. Mod. Phys.*, 1988, **60**, 781–850.
57 V. Balzani, A. Juris, M. Venturi, S. Campagna and S. Serroni, *Chem. Rev.*, 1996, **96**, 759–833.
58 J. L. Brédas, D. Beljonne, V. Coropceanu and J. Cornil, *Chem. Rev.*, 2004, **104**, 4971–5003.
59 L. Li, Q. Tang, H. Li, X. Yang, W. Hu, Y. Song, Z. Shuai, W. Xu, Y. Liu and D. Zhu, *Adv. Mater.*, 2007, **19**, 2613–2617.
60 H. Ebata, T. Izawa, E. Miyazaki, K. Takimiya, M. Ikeda, H. Kuwabara and T. Yui, *J. Am. Chem. Soc.*, 2007, **129**, 15732–15733.
61 G. Giri, E. Verploegen, S. C. B. Mannsfeld, S. Atahan-Evrenk, D. H. Kim, S. Y. Lee, H. A. Becerril, A. Aspuru-Guzik, M. F. Toney and Z. Bao, *Nature*, 2011, **480**, 504–508.
62 Y. Diao, B. C.-K. Tee, G. Giri, J. Xu, D. H. Kim, H. A. Becerril, R. M. Stoltenberg, T. H. Lee, G. Xue, S. C. B. Mannsfeld and Z. Bao, *Nat. Mater.*, 2013, **12**, 665–671.
63 M. W. Kim, S. Kwon, J. Kim, C. Lee, I. Park, J. H. Shim, I. S. Jeong, Y. R. Jo, B. Park, J. H. Lee, K. Lee and B. J. Kim, *Small*, 2020, **16**, 1906109.
64 D. Gentili, I. Manet, F. Liscio, M. Barbalinardo, S. Milita, C. Bettini, L. Favaretto, M. Melucci, A. Fraleoni-Morgera and M. Cavallini, *Chem. Commun.*, 2020, **56**, 1689–1692.
65 U. Herr, *Contemp. Phys.*, 2000, **41**, 93–104.
66 J. Baumgartner, A. Dey, P. H. H. Bomans, C. Le Coadou, P. Fratzl, N. A. J. M. Sommerdijk and D. Faivre, *Nat. Mater.*, 2013, **12**, 310–314.
67 A. O. F. Jones, B. Chattopadhyay, Y. H. Geerts and R. Resel, *Adv. Funct. Mater.*, 2016, 26, 2233–2255.
68 H. Chung and Y. Diao, *J. Mater. Chem. C*, 2016, 4, 3915–3933.
69 Y. Diao, K. M. Lenn, W. Y. Lee, M. A. Blood-Forsythe, J. Xu, Y. Mao, Y. Kim, J. A. Reinspach, S. Park, A. Aspuru-Guzik, G. Xue, P. Clancy, Z. Bao and S. C. B. Mannsfeld, *J. Am. Chem. Soc.*, 2014, **136**, 17046–17057.
70 S. S. Lee, S. B. Tang, D.-M. Smilgies, A. R. Woll, M. a Loth, J. M. Mativetsky, J. E. Anthony and Y.-L. Loo, *Adv. Mater.*, 2012, **24**, 2692–8.
71 B. Wedl, R. Resel, G. Leising, B. Kunert, I. Salzmann, M. Oehzelt, N. Koch, A. Vollmer, S. Duhm, O. Werzer, G. Gbabode, M. Sferrazza and Y. Geerts, *RSC Adv.*, 2012, **2**, 4404–4414.
72 E. K. Burnett, J. Ly, M. R. Niazi, L. Zhang, S. R. McCuskey, A. Amassian, D.-M. Smilgies, S. C. B. Mannsfeld and A. L. Briseno, *Adv. Mater. Interfaces*, 2018, **5**, 1701607.
73 J. Martín, M. Campoy-Quiles, A. Nogales, M. Garriga, M. I. Alonso, A. R. Goñi and M. Martín-González, *Soft Matter*, 2014, **10**, 3335.
74 J. Martín, M. Dyson, O. G. Reid, R. Li, A. Nogales, D. M. Smilgies, C. Silva, G. Rumbles, A. Amassian and N. Stingelin, *Adv. Electron. Mater.*, 2018, **4**, 1700308.
75 D. J. Gundlach, T. N. Jackson, D. G. Schlom and S. F. Nelson, *Appl. Phys. Lett.*, 1999, **74**, 3302–3304.
76 O. D. Jurchescu, J. Baas and T. T. M. Palstra, *Appl. Phys. Lett.*, 2004, **84**, 3061–3063.
77 Y. Diao, T. Harada, A. S. Myerson, T. Alan Hatton and B. L. Trout, *Nat. Mater.*, 2011, **10**, 867–871.
78 P. W. Carter and M. D. Ward, *J. Am. Chem. Soc.*, 1993, **115**, 11521–11535.